THE JOURNAL OF BIOLOGICAL CHEMISTRY VOL. 286, NO. 28, pp. 24626–24637, July 15, 2011

Comparison of a $preQ_1$ Riboswitch Aptamer in Metabolite-bound and Free States with Implications for Gene Regulation*[S]

Received for publication, February 11, 2011, and in revised form, April 29, 2011 Published, JBC Papers in Press, May 18, 2011, DOI 10.1074/jbc.M111.230375

Jermaine L. Jenkins[‡], Jolanta Krucinska[‡], Reid M. McCarty[§], Vahe Bandarian[§], and Joseph E. Wedekind[‡1]

From the [‡]Department of Biochemistry and Biophysics, University of Rochester School of Medicine and Dentistry, Rochester, New York 14642 and the [§]Department of Chemistry and Biochemistry, University of Arizona, Tucson, Arizona 85721

Riboswitches are RNA regulatory elements that govern gene expression by recognition of small molecule ligands via a high affinity aptamer domain. Molecular recognition can lead to active or attenuated gene expression states by controlling accessibility to mRNA signals necessary for transcription or translation. Key areas of inquiry focus on how an aptamer attains specificity for its effector, the extent to which the aptamer folds prior to encountering its ligand, and how ligand binding alters expression signal accessibility. Here we present crystal structures of the $preQ_1$ riboswitch from *Thermoanaerobacter tengcongensis* in the $preQ_1$-bound and free states. Although the mode of $preQ_1$ recognition is similar to that observed for $preQ_0$, surface plasmon resonance revealed an apparent K_D of 2.1 ± 0.3 nM for $preQ_1$ but a value of 35.1 ± 6.1 nM for $preQ_0$. This difference can be accounted for by interactions between the $preQ_1$ methylamine and base G5 of the aptamer. To explore conformational states in the absence of metabolite, the free-state aptamer structure was determined. A14 from the ceiling of the ligand pocket shifts into the $preQ_1$-binding site, resulting in "closed" access to the metabolite while simultaneously increasing exposure of the ribosome-binding site. Solution scattering data suggest that the free-state aptamer is compact, but the "closed" free-state crystal structure is inadequate to describe the solution scattering data. These observations are distinct from transcriptional $preQ_1$ riboswitches of the same class that exhibit strictly ligand-dependent folding. Implications for gene regulation are discussed.

Riboswitches are small, structured non-coding RNA molecules commonly located in the 5′ leader sequences of mRNA. These motifs are usually organized into a high affinity aptamer domain that binds a ligand and a downstream expression platform that possesses sequences necessary to direct transcription or translation (1). It has been estimated that as many as 4.1% of bacterial genes are controlled by such regulatory RNA elements (2, 3), with emerging evidence suggesting that some are susceptible to antimicrobial agents (4, 5).

At present, structures of nearly a dozen distinct classes of riboswitch aptamers have been solved in complex with their cognate ligands (6–8), but only three have been reported in the ligand-free state (8–11). Despite this disparity, comparisons of bound and free-state aptamers have provided valuable insight into the means by which metabolite binding transmits chemical binding information in the aptamer to distal expression platform signals that activate or attenuate transcription or translation (7, 11–13). Toward understanding this problem, we undertook a structural and functional analysis of a $preQ_1$ riboswitch from *Thermoanaerobacter tengcongensis* in the metabolite-bound and free states.

$PreQ_1$ is a metabolic intermediate in the synthetic pathway that produces the hypermodified guanine nucleotide, queuosine (Q)[2] (Fig. 1*A*), which is ubiquitous in the eubacterial and eukaryal domains of life (14). Whereas bacteria synthesize $preQ_1$ *de novo* in a multistep reaction that starts with GTP (15, 16), eukaryotes are devoid of this pathway and acquire Q from dietary sources or gut flora. A specialized enzyme called tRNA-guanine transglycosylase is then used to insert the Q base at position 34 of select tRNAs (17). The Q modification has been invoked as a source of translational fidelity and has been implicated in bacterial virulence (18) as well as tyrosine bioynthesis in animals (19). The prevalence of $Q^{(minus)}$-tRNA is correlated with neoplastic transformation and has been proposed as a metric to grade malignancies (20).

Bacterial genes involved in $preQ_1$ biosynthesis and cellular import were found to be regulated by a small, 34-nucleotide RNA motif known as the class 1 $preQ_1$ riboswitch (21). At present, this is the smallest known riboswitch aptamer, which was predicted to adopt a stem-loop structure followed by an A-rich tail (21). Subclasses of $preQ_1$ aptamers were labeled type I and II based on distinct consensus sequences, although their ligand specificities were reported to be the same (21). Subsequently, three independent laboratories described high resolution $preQ_1$ aptamer structures. The type I aptamer from *T. tengcongensis* was solved in the presence of $preQ_0$ (22) and is involved in translational regulation. Its organization is notable because a significant portion of the ribosome-binding site (RBS) is located

* This work was supported, in whole or in part, by National Institutes of Health Grants GM072623 (to V. B.) and GM063162 and RR026501 (to J. E. W.).

[S] The on-line version of this article (available at http://www.jbc.org) contains supplemental Figs. S1–S3.

The atomic coordinates and structure factors (codes 3Q50 and 3Q51) have been deposited in the Protein Data Bank, Research Collaboratory for Structural Bioinformatics, Rutgers University, New Brunswick, NJ (http://www.rcsb.org/).

[1] To whom correspondence should be addressed: 601 Elmwood Ave., Box 712, Rochester, NY 14642. Tel.: 585-273-4516; Fax: 585-275-6007; E-mail: joseph.wedekind@rochester.edu.

[2] The abbreviations used are: Q, queuosine; RBS, ribosome-binding site; SAXS, small angle x-ray scattering; SPR, surface plasmon resonance; CHESS, Cornell High Energy Synchrotron Source; SSRL, Stanford Synchrotron-Radiation Lightsource; DAP, 2,6-diaminopurine.

within the aptamer domain. By contrast, the type II aptamer from *Bacillus subtilis* was solved in complex with preQ$_1$ and exhibits spatially distinct aptamer and expression platform domains responsible for transcriptional regulation (23, 24). Nonetheless, both aptamer types are organized as H-type pseudoknots in which ~50% of bases engage in triples or quartet interactions (Fig. 1*B*). Solution analysis of type II aptamers from different species revealed folding that was strictly dependent on the presence of ligand with large structural changes observed upon preQ$_1$ binding (23, 25, 26). Global conformational changes have also been invoked for the thiamine pyrophosphate and glycine riboswitches (27–30).

In this investigation, we conducted crystallographic and solution small angle x-ray scattering (SAXS) analyses of the *T. tengcongensis* riboswitch in the preQ$_1$-bound and free states. A parallel SAXS analysis was conducted on the type II *Fusobacterium nucleatum* preQ$_1$ riboswitch, which has demonstrated ligand-dependent folding properties (25, 26). We then used surface plasmon resonance to measure the affinity of ligand interactions with the *T. tengcongensis* aptamer and to identify key affinity determinants as well as the basis for preQ$_1$ *versus* preQ$_0$ selectivity. The results suggest a mechanism of translational attenuation in which metabolite binding is coupled structurally to the solvent accessibility of the RBS. The apparent ability of *T. tengcongensis* aptamer to adopt a compact, folded conformation in the free state stands in sharp contrast to the type II transcriptional aptamers.

EXPERIMENTAL PROCEDURES

Preparation of RNA Aptamers and Crystallization—All RNA strands were synthesized by Dharmacon Inc. (Fayette, CO). The 33-mer used in crystallization (Fig. 1*B*) was deprotected, purified by HPLC, and desalted as described (31). The 34-mer aptamer from *F. nucleatum* harbored a double mutation (26) and was prepared similarly. Strands used for surface plasmon resonance (SPR) were prepared with a 5′-biotin modification and comprised the wild type sequence or point variations in Table 3.

Enzymatic Synthesis of PreQ$_0$ and PreQ$_1$—Synthetic preQ$_0$ was produced as described (15, 32). PreQ$_0$ was converted to preQ$_1$ by the *E. coli* enzyme QueF, which was purified as described (33). The reaction for the enzymatic conversion contained 0.050 M potassium phosphate (pH 7.4), 0.10 M KCl, 0.5 mM NADPH, 0.5 mM preQ$_0$, and 10 μM QueF in a final volume of 0.40 liter. The mixture was stirred gently for 8 h at 37 °C and filtered through a YM-10 (Amicon) membrane under $N_2(g)$ to remove QueF. The filtrate was lyophilized, resuspended in 0.20 liters of methanol, and stirred for 1 h to dissolve preQ$_1$. Undissolved material was removed by filtration, and methanol was removed by rotary evaporation until only a yellow solid remained. The solid was dissolved in 10 ml of water (pH 3.8) and loaded onto a 60-ml CM Sepharose Fast Flow column (2.6 × 11.3 cm; GE Healthcare) in water (pH 3.8). The column was rinsed with 0.10 liter of water (pH 3.8), and preQ$_1$ was eluted with a linear gradient extending to 0.5 M HCl in a volume of 0.50 liter. Fractions (5 ml) were collected and analyzed for the presence of preQ$_1$ by LC-MS using the following protocol. 25 μl of material was injected onto a 4.6 × 250-mm Eclipse XDB-C18 column (Agilent) that had been pre-equilibrated in water. PreQ$_1$ was eluted by developing the column with a gradient to 40% acetonitrile over 40 min at a flow rate of 0.3 ml/min. The elution was monitored by UV-visible and MS detection. UV-visible spectra were obtained from 220 to 500 nm using a ThermoFinnigan Surveyor photodiode array detector. Mass spectra were obtained in positive mode, scanning the m/z range of 100–300 atomic mass units using an electrospray ionization-equipped LCQ ThermoFinnigan Deca XP mass spectrometer. The instrument was set at a 6 V ionization energy and a 200 °C ion source temperature. Fractions containing preQ$_1$ were pooled, lyophilized, and dissolved in 1 ml of water. The concentration of preQ$_1$ was determined by UV absorbance using extinction coefficients published for 7-deazaguanine at pH 6.8 (34).

Crystallization and X-ray Structure Determination—The free-state riboswitch was crystallized by suspending lyophilized RNA in 0.010 M sodium cacodylate buffer, pH 7.0, to a concentration of 0.5 mM. A total of 20 μl was heated to 65 °C for 2 min before cooling to 30 °C in an aluminum block, followed by the addition of $MgCl_2$ to a final concentration of 0.010 M. The sample was heated again to 65 °C and held for 3 min, followed by slow cooling in a 0.5-liter water bath to 20 °C over 2 h. Crystallization trials were set up using hanging drop vapor diffusion in which 2 μl of RNA was added to 2 μl of mother liquor comprising 2.0 M Li_2SO_4, 0.050 M MES, pH 6.0, 0.003 M $MgSO_4$ and 0.002 M spermine at 20 °C. Crystals grew as hexagonal rods to 0.4 × 0.15 × 0.15 mm in 6–8 weeks. Metabolite-bound crystals were prepared as described (22) using preQ$_1$ in place of preQ$_0$. Crystals were cryoprotected in equal mixtures of Paratone-N and silicone oils (Hampton Research) and flash frozen (22).

X-ray diffraction data were collected on site at the Cornell High Energy Synchrotron Source (CHESS) (Ithaca, NY), and remotely at the Stanford Synchrotron-Radiation Lightsource (SSRL) (Menlo Park, CA) using the *Blu-Ice* and *Web-Ice* interfaces (35). Intensity data were reduced using *HKL2000* (36). Structures were solved by difference Fourier methods in PHENIX (37) using the preQ$_0$ structure (Protein Data Bank entry 3gca) as a starting model. Both structures were subjected to manual rebuilding in COOT (38). The free-state structure was subjected to Cartesian simulated annealing with rebuilding into composite omit maps. Intensity and refinement statistics are provided in Table 1. Figure graphics were generated in PyMOL (39). Solvent accessibility was calculated with AREAIMOL (40).

SAXS—Experiments were conducted at the G1 station of CHESS. Using a wavelength of 1.29 Å, scattered X-rays were recorded on a CCD detector at a sample-to-detector distance of 94.2 cm. This configuration gave an accessible q range from 0.025 to 0.35 Å^{-1}, where $q = 4\pi\sin\theta\ \lambda^{-1}$, in which 2θ is the scattering angle and λ is the radiation wavelength. Samples of the preQ$_1$ aptamer were prepared in the presence or absence of metabolite in 0.010 M sodium cacodylate, pH 6.0, with 0.010 M $MgCl_2$. Three sample concentrations were utilized, including 0.075, 0.20, and 0.55 mM. Microcentrifuged samples were transferred to disposable cells (41) held at 20 °C. Buffer blanks were collected for each cell. Exposures were recorded as 3 × 3 s followed by 3 × 9 s series. Scattering data for the 3 × 9 s exposures were integrated by Data Squeeze, version 2.20 (P. Heiney)

to yield the respective one-dimensional intensity profiles. No evidence of radiation damage was observed based on a comparison of initial *versus* final exposures. Buffer corrections and extrapolation to zero concentration were accomplished using PRIMUS (43); it has been noted that extrapolation to infinite dilution can circumvent problems with interparticle interference that can cause inaccurate measurements (44). Kratky plots were generated for the full range of data, and Guinier plots were calculated with PRIMUS. GNOM was used to produce the paired distance distribution functions, which were optimized to meet visual perception criteria as described (45). Dimensions of crystal structures and fits between experimental and crystallographic scattering profiles were calculated using CRYSOL (46); additional dimensions were obtained by use of MOLEMAN (47). Relevant SAXS parameters are reported in Table 2.

SPR—NeutrAvidin-conjugated CM5 chips were prepared on a Biacore T100 instrument (Biacore Inc., Piscataway, NJ) using reagents from the manufacturer. Biotinylated free-state preQ$_1$ aptamers and variants thereof (Table 3) were suspended in running buffer (0.010 M sodium cacodylate, pH 7.0, and 0.003 M $MgCl_2$) to a concentration of 400 nM. RNA aptamers were injected over NeutrAvidin-conjugated flow cells to give a surface density of 3800–4000 response units, with the reference flow cell having only NeutrAvidin. For kinetic experiments, the association phase consisted of 180-s injections of preQ$_1$ or preQ$_0$ conducted at concentrations ranging from 1 to 250 nM at 75 μl/min; dissociation was monitored for 600 s. Regeneration was conducted using 3 M guanidine HCl for 180 s followed by a 120-s incubation in running buffer flowing at 30 μl/min. Equilibrium binding experiments were carried out as follows. Injections of metabolite lasted for 240 s at 30 μl/min and were conducted with concentrations ranging from 0.470 to 400 μM. A dissociation phase of 400 s ensued in running buffer. Regeneration was accomplished using 3 M guanidine HCl for 90 s, followed by a 160-s stabilization period in running buffer at 30 μl/min. All measurements were made in duplicate at 25 °C with a data collection rate of 10 Hz. Experimental data were processed using Biacore T100 Evaluation software version 2.2 (GE Healthcare) and the double referencing method (48) to remove instrumental and bulk shift effects. The buffer-subtracted sensorgrams for the kinetic binding data were then fit to a 1:1 binding interaction model to determine the rate constants (k_{on} and k_{off}) and the apparent equilibrium binding constant (K_D). To evaluate the steady-state equilibrium binding data, the response during the equilibrium binding phase (R_{eq}) was calculated by averaging the response over 5 s just before the end of the metabolite injection. Data were fit using non-linear curve fitting using PRISM4 (GraphPad, Inc.) to a one-site binding equation to determine K_D.

RESULTS

Quality Indicators and Overall Fold of the PreQ$_1$-bound Riboswitch Aptamer—To understand the basis of metabolite specificity and gene regulation by the class 1, type I *T. tengcongensis* preQ$_1$ translational riboswitch, we undertook a structure determination in the presence of the primary target ligand, preQ$_1$ (Fig. 1*A*). The entire 33-mer RNA aptamer was observed in electron density maps as well as the preQ$_1$ ligand, whose omit

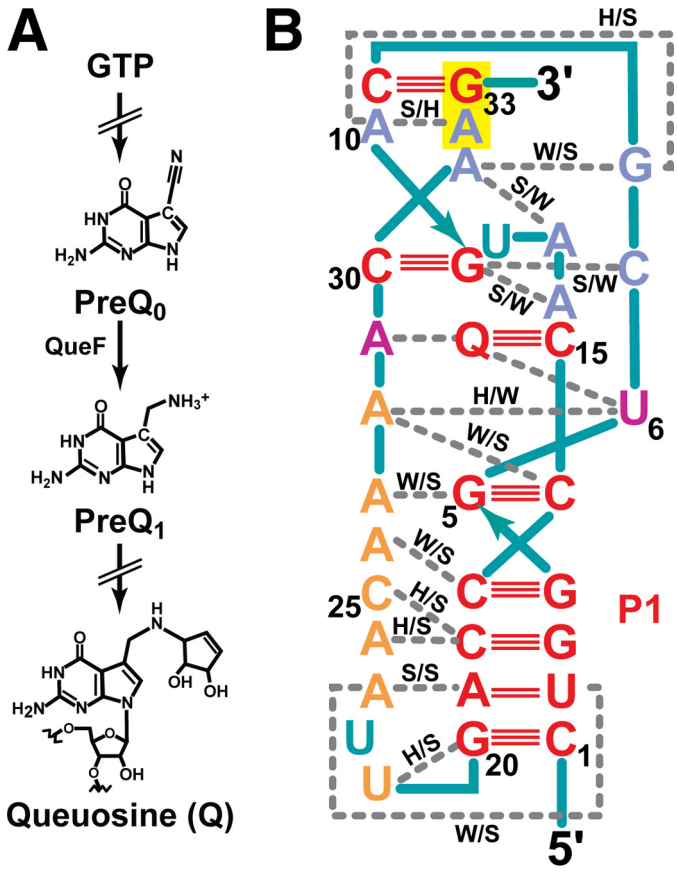

FIGURE 1. **Schematic diagrams of queuosine-precursor metabolites and preQ$_1$ riboswitch organization.** *A*, relationship between GTP and the hypermodified base queuosine, whose synthesis proceeds through preQ$_0$ (7-cyano-7-deazaguanine) and preQ$_1$ (7-aminomethyl-7-deazaguanine) intermediates via the nitrile reductase QueF. In eubacteria, TGTase (tRNA transglycosylase) inserts preQ$_1$ into the wobble position of specific tRNAs, where it is modified further to give Q (14). *B*, secondary structure and nucleotide interaction diagram for the *T. tengcongensis* aptamer adapted from Ref. 22. The *color code* is as follows. *Red*, bases involved in Watson-Crick pairs (*triple* or *double solid lines*); *orange*, A-rich region; *purple*, strictly conserved, non-canonical base interactions with metabolite; *slate*, decaloop bases engaged in non-canonical pairing and base triples; *teal bases* are bulged. *Q*, the metabolite. Interactions are as follows. *W*, Watson-Crick face; *S*, sugar edge; *H*, Hoogsteen edge. The RBS is highlighted in *yellow*.

electron density map is representative of the overall quality of the model (Table 1 and Fig. 2*A*). The hydrogen bonding pattern, global fold, and location of the metabolite closely matched features reported previously for the preQ$_0$-bound state (Figs. 1*B* and 2*B*) (22). The quality of the 2.75 Å resolution preQ$_1$-bound structure is indicated by its R_{work} and R_{free} values of 21.0 and 25.2%, respectively (Table 1), which are substantially lower than the preQ$_0$-aptamer complex, whose R_{work} and R_{free} values were 24.5 and 27.2% (22). Despite identical diffraction resolutions, *B*-factors for the preQ$_1$-bound state were 57 Å^2 for RNA atoms and 48 Å^2 for preQ$_1$ (Table 1) as compared with *B*-factors of 76 Å^2 for RNA atoms and 58 Å^2 for preQ$_0$ of the preQ$_0$-bound state.

Quality Indicators and Overall Fold for the Free-state Aptamer—To understand the conformational changes involved in RNA-mediated gene regulation by sequestration of the RBS, we determined the ligand-free *T. tengcongensis* aptamer structure (Fig. 2*C*). Compared with the preQ$_1$-bound state, free-state crystals showed a 7.6% increase in the unit cell

TABLE 1
X-ray data reduction and refinement statistics

	PreQ$_1$-bound + Mg^2	Free state (Mg^{2+} only)
X-ray data reduction statistics		
Protein Data Bank accession code	3Q50	3Q51
Beamline	CHESS A-1	SSRL 9–2
Wavelength (Å)	0.98	0.98
Space group	$P6_322$	$P6_322$
Unit cell (Å)	$a = 110.8$, $c = 59.6$	$a = 116.6$, $c = 57.9$
Total observations	38,982	41,267
Unique observations	6041	5771
Resolution (Å)	22-2.75 (2.80-2.75)[a]	27.8-2.85 (2.95-2.85)
Completeness (%)	99 (96)	99.2 (100)
⟨Redundancy⟩	6.5 (5.1)	7.2 (8.4)
$I/\sigma(I)$	24.7 (2.1)	20.6 (6.7)
R_{sym} (%)[b]	7.1 (43.6)	7.5 (35.7)
Refinement statistics		
$R_{cryst}/R_{work}/R_{free}$ (%)[c,d,e]	21.4/21.0/25.2	23.1/22.6/27.2
Geometry		
Root mean square bonds (Å)	0.007	0.006
Root mean square angles (degrees)	1.689	0.844
Coordinate error (Å)	0.35	0.40
No. of atoms/*B*-factors		
RNA	702/56.6 Å^2	680/56.7
Metabolite	13/47.7 Å^2	None
SO_4^{2-}	20/67.5 Å^2	5/51.8 Å^2
Mg^{2+}	None	1/60.3 Å^2
Anisotropy correction	B11:12.6 B33:−25.2	B11:10.6 B33:−21.2

[a] Values in parentheses represent high resolution statistics.
[b] $R_{sym} = [\Sigma|I(h)_j - \langle I(h)\rangle|/\Sigma|I(h)_j|] \times 100$, where $I(h)_j$ is the intensity of the *j*th reflection of type *h*, and $\langle I(h)\rangle$ is the average intensity of a reflection of type *h*.
[c] R_{cryst} represents a final cycle of refinement without cross-validation using the residual target and all reflections.
[d] $R_{work} = [\Sigma_{hkl}|(F_o) - k(F_c)|]/[\Sigma_{hkl}|(F_o)|] \times 100$, where *k* is a scale factor and the test set has been removed.
[e] R_{free} is defined as the R_{work} calculated for 9% of the x-ray data selected randomly and excluded from refinement.

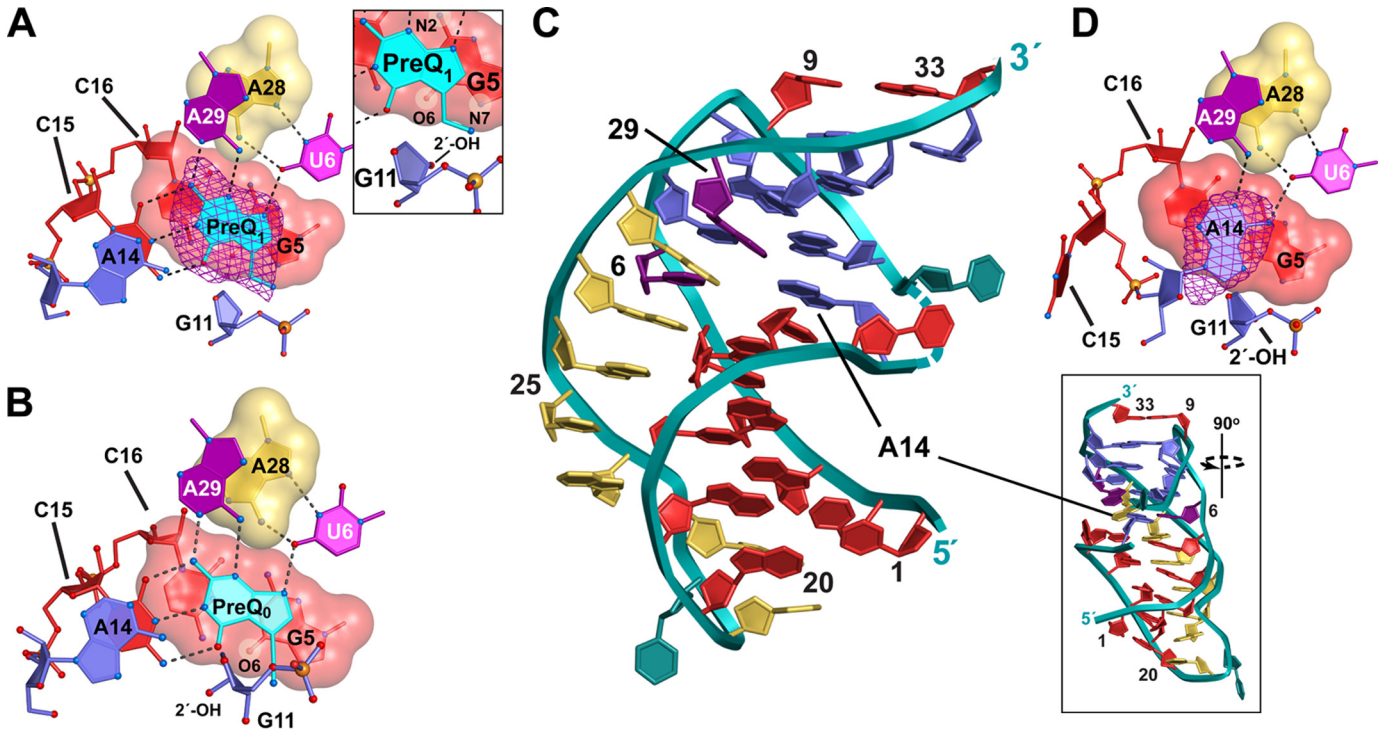

FIGURE 2. **Schematic representations of the preQ$_1$ riboswitch in the free and preQ$_1$-bound states.** *A*, aptamer interactions with preQ$_1$ looking down the helical axis of the riboswitch. The "floor" of the binding pocket is shown as a *space-filling model*; putative hydrogen bonds are shown as *dashed lines*. The location of the ligand is indicated by an averaged "kicked" (66) or AK ($mF_o - DF_c$) omit electron density map with σA weighting contoured at 4σ; the ligand (*cyan*) was removed from the phase calculation. *Inset*, close-up view of the preQ$_1$ methylamine in relation to the G11 2′-OH group and the G5 O6 keto moiety. Neighboring groups of G5 are highlighted with a *semitransparent circle* and labeled; the electron density has been removed for clarity. *B*, aptamer interactions with preQ$_0$ based on Protein Data Bank entry 3cga as described previously (22). *C*, *ribbon diagram* of the free-state riboswitch. The phosphate backbone is depicted as a *teal ribbon* with bases *colored* as in Fig. 1*B*; *inset*, a view rotated 90° to accentuate the location of A14 within the ligand-binding pocket. *D*, schematic diagram depicting A14 of the free-state structure; the purine base was removed from the phase calculation to generate an AK ($mF_o - DF_c$) omit map as in *A*.

volume (Table 1), suggestive of significant structural differences. Although the overall fold of the free-state structure is comparable with the compact 48 Å × 28 Å × 15 Å preQ$_1$-bound state, changes occurred in the RNA backbone flanking the metabolite-binding pocket. No electron density was observed for A13 of the decaloop, indicated as a *dashed line* in

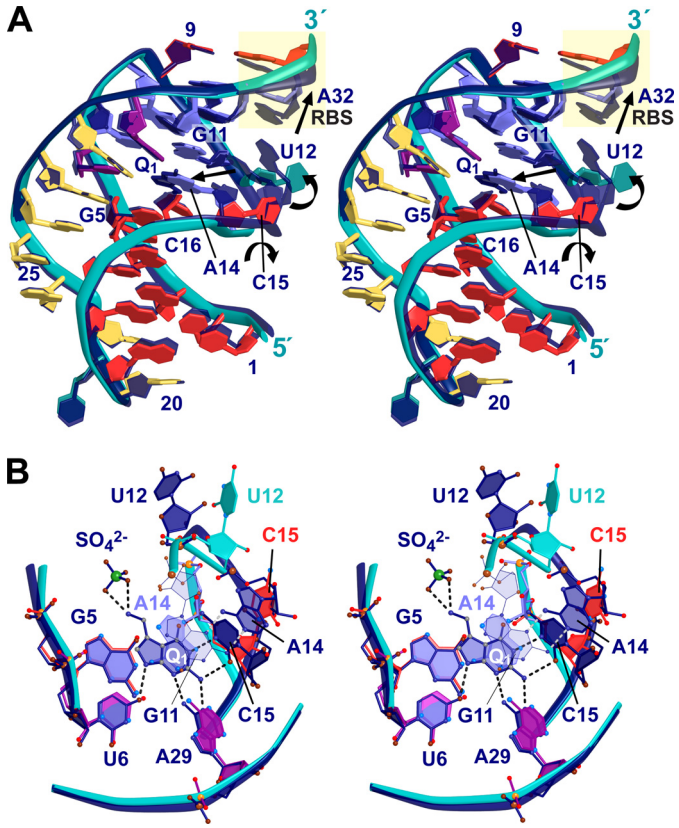

FIGURE 3. **All-atom superposition of the respective free-state and ligand-bound structures.** *A*, schematic stereo view of the global, free-state structure (*colored* as in Fig. 2) superimposed upon the preQ$_1$-bound structure (*dark blue*) using LSQKAB (42). *Black arrows* indicate the movements of bases in the preQ$_1$-bound structure relative to those of the free state. The start of the ribosome-binding site at A32 is labeled *RBS*. The RBS portion of the aptamer is highlighted in *yellow*. The preQ$_1$ metabolite is labeled *Q$_1$*. A *ribbon* passing through the phosphate backbone is shown in *teal* (free state) and blue (preQ$_1$-bound). *B*, close-up stereo diagram of *A* (rotated +90° along the *x* axis) depicting the superposition of select decaloop nucleotides. Putative hydrogen bonds to preQ$_1$ in the ligand-bound structure are drawn as *broken lines*. Nucleotides that superimpose with a root mean square deviation of >2.0 Å are labeled twice for the respective ligand-bound (*blue*) or free state (*colored* as in Fig. 2*C*) structures. Base G11 was rendered with *thin bonds* for clarity; here only the preQ$_1$-bound state is shown because of its close similarity to the free-state structure.

the backbone of Fig. 2*C*, and the quality of the electron density in this region was generally poorer than that of either ligand-bound state. The overall RNA *B*-factors were comparable at 57 Å^2, but the R_{work} and R_{free} values were slightly worse than the preQ$_1$-bound state (Table 1). Significantly, the electron density was of sufficient quality and resolution to observe conformational changes in the decaloop at C15 and A14 that are consistent with changes resulting from ligand-free crystallization as opposed to crystal packing because this area is devoid of lattice contacts. Reduced bias omit-electron density maps, such as that calculated for the A14 base of the free-state structure (Fig. 2*D*), indicate the quality of the model in this region. The level of change relative to the coordinate error (Table 1) is sufficiently large to permit a meaningful structural comparison on both global and local levels.

Comparison of the PreQ$_1$-bound and Free-state Crystal Structures Reveals a Network of Localized Conformational Changes—To contrast the preQ$_1$-bound and free state aptamers, an all-atom superposition was conducted (Fig. 3*A*). Although only a few nucleotides differed significantly in their relative positions, this was sufficient to elevate the root mean square displacement of atoms to 1.7 Å. The maximum displacement was 7.4 Å, which corresponded to the N1 imino of A14. The nucleotide at this position rotates out of a stable G11 to A14 (N3-amino amino-N1) pair flanking the ligand pocket to occupy the preQ$_1$ binding site (Fig. 3*B*, compare *dark blue A14* to *light blue A14*). Other pronounced changes cluster in the pseudoknotted decaloop surrounding the preQ$_1$ binding site. C15 rotates away from the binding pocket, a 6.6-Å movement of N3, from a location where it base-pairs with preQ$_1$ (Fig. 2, *A versus D*, and Fig. 3, *dark blue C15 versus red*). By contrast, U12 shifts by 4.4 Å toward the binding pocket closer to the position vacated by A14. Finally, base A32 moves away from the binding pocket in the free-state structure by 2.3 Å. These changes appear interconnected to the A14 shift, which has the effect of eliminating the continuous base stack that links A32 and G33 of the RBS to preQ$_1$ in the aptamer core in the ligand-bound state.

Molecular Recognition of PreQ$_1$ and Closure of the Binding Pocket in the Free State—Although the mode of preQ$_0$ binding has been described for the *T. tengcongensis* riboswitch aptamer (22), the mode of preQ$_1$ binding has remained uncertain until now. The compact architecture of the aptamer buries 330 of 337 Å^2 of the preQ$_1$ metabolite fortifying the core structure by generating a network of continuously stacked bases that join the RBS at the "top" of the aptamer to the P1 stem (Figs. 1*B* and 3*A*). Like preQ$_0$, the Watson-Crick face of preQ$_1$ is "read out" by C15 (Fig. 2, *A* and *B*), and conserved bases U6 and A29 recognize the minor groove edge of both metabolites. The modified guanine base of the metabolite stacks between the G5-C16 base pair of the P1 stem (Fig. 2*A*) and bases G11 and A14 (Fig. 3). These interactions have been referred to as the respective "floor" and "ceiling" of the binding pocket (22). However, in the absence of metabolite, the pocket adopts a "closed" conformation whereby binding to preQ$_1$ is blocked by A14, which spatially overlaps the ligand-binding site (Fig. 3*B*) and pairs with key bases involved in ligand recognition, most notably U6 and A29 (Fig. 2*D*). Because A14 forms part of the binding pocket ceiling, its shift in the free state effectively collapses the ligand recognition site and directly increases the solvent accessibility of the RBS from 468 to 511 Å^2, which starts at position A32 of the aptamer (Figs. 1*B* and 3*A* and supplemental Fig. S1).

Small Angle X-ray Scattering Analysis of the T. tengcongensis and F. nucleatum PreQ$_1$ Aptamers—An important question regarding the observed preQ$_1$-bound and free state crystal structures is whether they are consistent with (i) the compactness and (ii) the conformations present in the solution state. To address these questions, we subjected the *T. tengcongensis* riboswitch to SAXS analysis. We also examined the *F. nucleatum* 34-mer class 1, type II preQ$_1$ aptamer as a control, which was chosen for its pronounced ligand-dependent folding (25, 26).

The results revealed smooth intensity distributions with gently changing slopes for both aptamer types (Fig. 4*A*). Sudden upturns or downturns were not observed, consistent with an absence of aggregation and interparticle repulsion, respectively (49). Visual comparisons indicated that the free-state *F. nucleatum* aptamer has a more negative slope at low *q* than the matched sample prepared in the presence of preQ$_1$ (Fig. 4*A*,

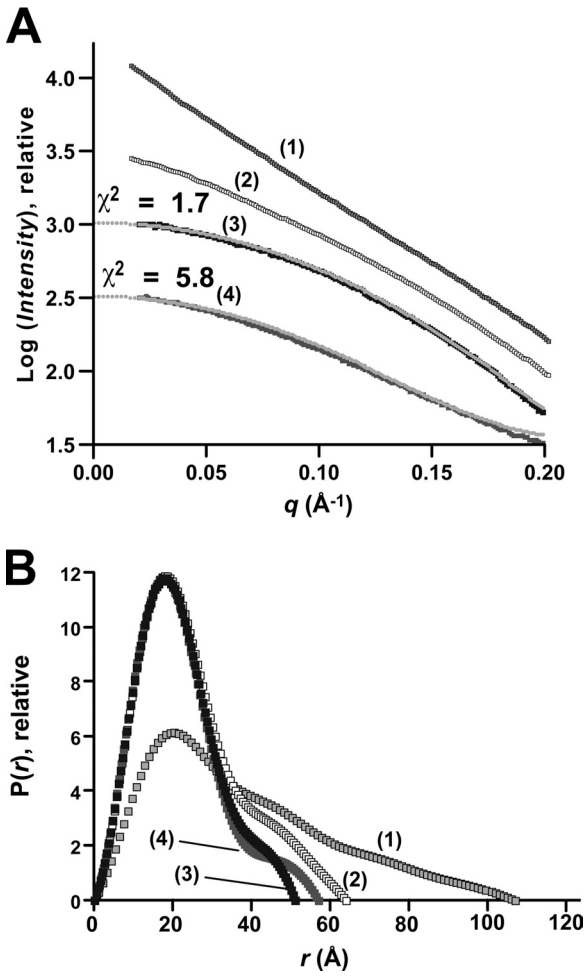

FIGURE 4. **Small angle x-ray scattering analysis of preQ$_1$ riboswitches from *T. tengcongensis* and *F. nucleatum* in metabolite-bound and free states.** *A*, scattering profiles (*thick lines*) derived from experimental measurements and those calculated from *T. tengcongensis* crystal structures (*thin gray lines*) in Table 1. The samples are free-state *F. nucleatum* with 10 mM Mg^{2+} (*1*), preQ$_1$-bound *F. nucleatum* with 10 mM Mg^{2+} (*2*), preQ$_1$-bound *T. tengcongensis* with 10 mM Mg^{2+} (*3*), and free-state *T. tengcongensis* with 10 mM Mg^{2+} (*4*). The agreement between the scattering profiles from the experimental SAXS data and crystallographic coordinates of the respective *T. tengcongensis* preQ$_1$-bound and free-state crystal structures is given by χ^2 as defined by CRYSOL (46). *B*, comparison of the paired distance distribution plots, *P*(*r*), for the samples in *A*. The real-space R_g^P and maximum intraparticle distance, r_{max}, from these functions are reported in Table 2. The functions were scaled relative to a reference according to the integrated areas of each respective curve.

TABLE 2
Solution dimensions from small angle x-ray scattering

	R_g^G	R_g^P	r_{max}
	Å	Å	Å
Wild type preQ$_1$ + Mg^{2+}	16.6 ± 0.02	16.5 ± 0.01	51 ± 5
Wild type preQ$_0$ + Mg^{2+}	16.9 ± 0.02	16.9 ± 0.01	57 ± 6
Wild type Mg^{2+}	17.0 ± 0.02	17.0 ± 0.01	57 ± 6
F. nucleatum preQ$_1$ + Mg^{2+}	19.3 ± 0.03	19.3 ± 0.01	64 ± 6
F. nucleatum Mg^{2+}	31.0 ± 0.07	30.9 ± 0.02	107 ± 11
Crystal coordinates, preQ$_0$/Q$_1$		16.9[a]	50[b]
Crystal coordinates, free state		17.0[a]	52[b]

[a] Calculation considers the solvent shell from CRYSOL (46).
[b] From MOLEMAN (47), including 1.6 Å for a monolayer shell of water on the molecular surface (65).

curve 1 versus curve 2). In contrast, the *F. nucleatum* sample in the presence of preQ$_1$ is more similar to the *T. tengcongensis* samples (Fig. 4*A*, *curves 2–4*). Based on visual criteria (49), the quality of the scattering profiles was deemed suitable for dimensional analysis.

Comparison of Ligand-induced Compaction of PreQ$_1$ Aptamers—To evaluate the degree to which the *T. tengcongensis* translational riboswitch undergoes ligand-dependent compaction, we used three criteria: (i) reduction of radius of gyration (R_g) values derived from both Guinier plots (R_g^G; supplemental Fig. S2*B*) and paired distance distribution functions (R_g^P; *i.e.* *P*(*r*) plots in Fig. 4*B* and supplemental Fig. S2*C*); (ii) reduction of the longest interatomic distance r_{max} in a sample from *P*(*r*) functions; and (iii) the shapes of Kratky plots, which show distinct dependences of momentum transfer-weighted intensity *versus q* for folded *versus* unfolded polymers (50) (supplemental Fig. S2*D*).

Significant differences in ligand-dependent compaction were observed between the *F. nucleatum* and *T. tengcongensis* riboswitch aptamers. The *F. nucleatum* "control" aptamer in the absence of ligand had a significantly larger R_g of 31.0 Å and longer r_{max} of 107 ± 11 Å compared with its preQ$_1$-bound state, in which the R_g was 19.3 Å and r_{max} was 64 ± 6 Å (Fig. 4*B* and Table 2). The broad, heavy tailed Kratky plots of the free-state *F. nucleatum* aptamer were consistent with partial folding in the absence of preQ$_1$ (supplemental Fig. S2*D*), whereas the bell-shaped, light-tailed profile of the preQ$_1$-bound aptamer was characteristic of a well folded polymer (supplemental Fig. S2*D*) (49, 50). Conversely, the *T. tengcongensis* aptamer appeared as compact in the free state with R_g^G = 17.0 Å and r_{max} = 57 ± 6 Å, as it is in the preQ$_1$- and preQ$_0$-bound states in which the respective R_g^G and r_{max} values were 51 ± 5 and 16.6 Å and 57 ± 6 and 16.9 Å (Table 2). Kratky profiles for each of the *T. tengcongensis* samples were comparable with the preQ$_1$-bound *F. nucleatum* aptamer, indicative of folded RNA (supplemental Fig. S2*D*).

Comparison of Crystal Structures with Solution SAXS Data—We then asked whether our crystal structures were representative of solution dimensions and conformational states. The experimentally measured R_g^P and r_{max} values were in reasonable agreement with those calculated from the respective preQ$_1$-bound, preQ$_0$-bound, and free-state crystal structures but with notable differences. The best agreement corresponded to the preQ$_1$-bound state in which the crystal structure R_g^P and r_{max} values were 16.9 and 50 Å *versus* the solution R_g^P and r_{max} values of 16.5 and 51.5 Å (Table 2). The solution R_g^P values for the preQ$_0$-bound and free-state samples agreed exactly with crystal structures at 16.9 and 17.0 Å, respectively (Table 2). However, the corresponding solution r_{max} values for the preQ$_0$-bound and free-state samples were each 57 Å, which is longer than the corresponding crystal structures, whose values were 50 and 52 Å, respectively. This finding may be the result of greater mobility in solution or conformational restraints imposed on the coordinates by the crystal lattice, which can only accommodate an r_{max} of ~52 Å (discussed below).

To assess the agreement between the intensity profiles calculated from crystal structures in Table 1 *versus* those corresponding to the experimental data, we calculated χ^2 values (46). The results revealed that the preQ$_1$-bound crystal structure has a χ^2 value of 1.7, indicating reasonable agreement between the

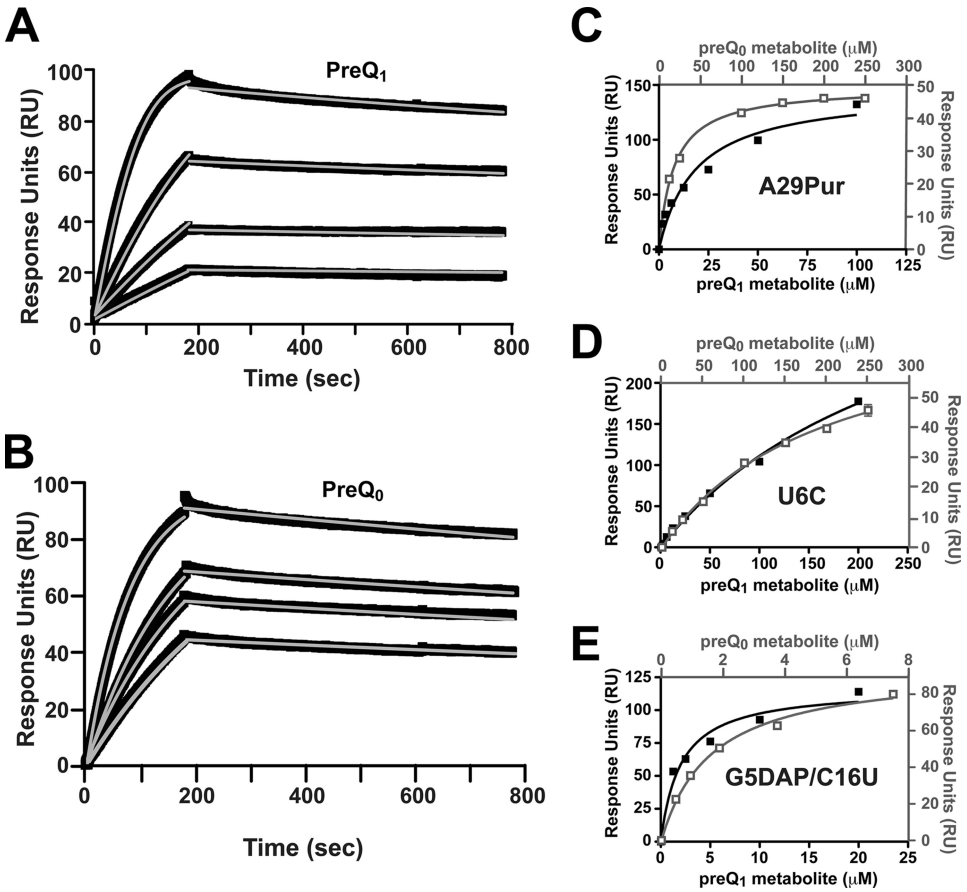

FIGURE 5. **Kinetic and affinity analysis of the *T. tengcongensis* riboswitch aptamer for preQ$_1$ and preQ$_0$.** *A*, representative surface plasmon resonance sensorgram for preQ$_1$ interactions with the wild type aptamer. *B*, representative surface plasmon resonance sensorgram for preQ$_0$ interactions with the wild type aptamer. The *thick black lines* represent the buffer-subtracted data, and *gray lines* are the global fit obtained from a 1:1 binding model based on the experimental data. The resulting k_{on} and k_{off} rates and the apparent equilibrium K_D values are reported in Table 3. *C*, A29Pur mutant response at equilibrium (R_{eq}) plotted against the concentration of preQ$_1$ or preQ$_0$. *D*, the U6C mutant as described in *C*. *E*, the G5DAP/C16U double mutant as described in *C*. The plots of R_{eq} correspond to preQ$_1$ data points (*filled squares*) or preQ$_0$ data points (*open squares*); *error bars* are shown. The equilibrium binding constant K_D was determined for each metabolite by curve fitting (*black* or *gray lines*) to the respective metabolite R_{eq} data points as described under "Experimental Procedures." The apparent K_D values are reported in Table 3.

atom model and the solution conformation (11). In contrast, the free-state crystal structure yielded a χ^2 of 5.8. Deviations in the intensity fit can be seen at several distinct points along the curve, especially a medium and high q (Fig. 4*A*, *curve 4*). This level of discrepancy is strong evidence that the crystallographic model is insufficient to describe the solution conformational ensemble and that differences between the bound and free states are more complex than suggested by a comparison of the corresponding crystal structures, despite similarities in compactness demonstrated by R_g^P and r_{max}.

Kinetics and Affinity Constants for PreQ$_1$ and PreQ$_0$ Binding to the T. tengcongensis Aptamer—PreQ$_0$ and preQ$_1$ differ by substitution of a cyano group for a methylamine (Fig. 1*A*). To evaluate the kinetics and thermodynamics of ligand binding, we measured the rates of binding and dissociation to the *T. tengcongensis* aptamer using surface plasmon resonance (Fig. 5, *A* and *B*). The results revealed that preQ$_1$ binds with an on-rate of $7.77 \times 10^4\ M^{-1}\ s^{-1}$, which is 12-fold faster than the on-rate for preQ$_0$ (Table 3). Both metabolites exhibited similar off-rates at $1.53 \times 10^{-4}\ s^{-1}$ and $2.22 \times 10^{-4}\ s^{-1}$, respectively. The k_{on} for the *T. tengcongensis* aptamer is 8-fold slower than preQ$_1$ binding to the *F. nucleatum* 34-mer aptamer, but k_{off} for the *F. nucleatum* aptamer is $>10^3$-fold faster (25). The preQ$_1$ on-rate of the *T. tengcongensis* aptamer falls into a range of values reported for other translational riboswitches, including the *Escherichia coli* thiamine pyrophosphate aptamer at $8.66 \times 10^4\ M^{-1}\ s^{-1}$ (51) and the *Vibrio vulnificus* adenine aptamer at $3.75 \times 10^4\ M^{-1}\ s^{-1}$ (52). By contrast, the off-rate of the *T. tengcongensis* aptamer is 2 orders of magnitude slower than the TTP (0.043 s^{-1}) and adenine (0.017 s^{-1}) aptamers. At present, the slowness of the *T. tengcongensis* off-rate is surpassed only by the *Vibrio cholerae* c-di-GMP riboswitch, a transcriptional regulator whose off-rate is 850-fold slower (53).

The *T. tengcongensis* aptamer apparent equilibrium dissociation constant (K_D) was 2.05 ± 0.29 nM for preQ$_1$ and 35.10 ± 6.07 nM for preQ$_0$. The magnitude and affinity trends mirror values reported previously for these metabolites during an analysis of a longer *B. subtilis* aptamer (20 and 100 nM, respectively) using equilibrium dialysis (21). By contrast, the *F. nucleatum* aptamer showed a K_D of 283 nM for preQ$_1$, making the *T. tengcongensis* aptamer a significantly tighter preQ$_1$ binder than either of the transcriptional riboswitches in its class.

TABLE 3
Affinity constants of the *T. tengcongensis* preQ$_1$ riboswitch and its variants for metabolites

	$k_{on} \times 10^4$	S.E. $\times 10^2$	S.D. $\times 10^4$	$k_{off} \times 10^{-4}$	S.E. $\times 10^{-6}$	S.D. $\times 10^{-4}$	K_D[a]	S.D.	$t_{1/2}$	K_{rel} (K_D(mut)/ K_D(WT preQ$_1$))
	$M^{-1}\,s^{-1}$			s^{-1}			nM		h	
Wild type preQ$_1$	7.77	3.55	3.45	1.53	1.00	0.47	2.05	0.29	1.4	1
Wild type preQ$_0$	0.65	0.27	0.13	2.22	1.04	0.14	35.10	6.07	0.9	17
G11dG preQ$_1$	8.47	2.94	3.71	1.42	0.96	0.58	1.69	0.22	1.6	0.8
G11dG preQ$_0$	0.65	0.20	0.10	1.83	1.07	0.27	28.90	7.7	1.1	14
G5DAP/C16U preQ$_1$	—[b]	—	—	—	—	—	2.01×10^3	3.32×10^2	—	981
G5DAP/C16U preQ$_0$	—	—	—	—	—	—	1.63×10^3	1.17×10^2	—	795
U6C preQ$_1$	—	—	—	—	—	—	$>2.74 \times 10^5$	3.05×10^4	—	—
U6C preQ$_0$	—	—	—	—	—	—	$>1.99 \times 10^5$	2.01×10^4	—	—
A29Pur preQ$_1$	—	—	—	—	—	—	1.84×10^4	3.34×10^3	—	8976
A29Pur preQ$_0$	—	—	—	—	—	—	1.80×10^4	8.42×10^2	—	8781

[a] Here we use the nomenclature K_D with the clarification that it is an apparent K_D.
[b] —, not determined (apparent K_D obtained from equilibrium analysis) or an estimate that precludes K_{rel} calculation.

Using Mutagenesis and SPR to Probe T. tengcongensis Riboswitch Aptamer Binding to Metabolites—Specific predictions about the molecular interactions between the *T. tengcongensis* aptamer and preQ$_1$ or preQ$_0$ can be proposed based on new and prior structural observations (Fig. 2, *A* and *B*) (22). To test the importance of key aptamer functional groups consistent with hydrogen bonding to preQ$_1$ or preQ$_0$ and to differentiate the modest difference in ligand-binding affinity, we undertook an SPR analysis of specific site-directed mutants that were placed into two categories: (i) those that recognize guanine-like features, and (ii) those that promote preQ$_1$ binding but not necessarily preQ$_0$.

Mutagenesis of T. tengcongensis Aptamer Bases That Recognize Guanine-like Features Shared by PreQ$_1$ and PreQ$_0$—The first class of mutants examined were those predicted to interact with the guanine-like features held in common by preQ$_1$ and preQ$_0$. Prior analysis indicated that position C15 (*T. tengcongensis* numbering) is a universally conserved base in the class 1 preQ$_1$ aptamer family and that modifications to this base ablated preQ$_1$ binding or could be used to alter ligand specificity in a manner consistent with Watson-Crick pairing (21). This finding was corroborated subsequently by three independent structure determinations (22–24), which also revealed the locations of other key groups involved in metabolite recognition. Of special importance are universally conserved bases U6 and A29 because they each recognize the same minor groove edge features of preQ$_1$ and preQ$_0$ (Fig. 2, *A* and *B*) (22).

Our mutagenesis results revealed that the A29Pur and U6C variants each have detrimental effects on preQ$_1$ and preQ$_0$ binding but to varying extents (Fig. 5, *C* and *D*). The A29Pur variant is devoid of an exocyclic amine and was predicted to eliminate a single hydrogen bond to the metabolites (Fig. 2, *A* and *B*). The resulting K_D values were 18.4 μM for preQ$_1$ and 18.0 μM for preQ$_0$, which is nearly 9000-fold worse than wild type binding to preQ$_1$ (Table 3). Loss of the A29 amine also ablates a core folding interaction with the O_2 keto of C7 (not shown) that may account for a loss in binding affinity for both ligands that is significantly greater than removal of a single hydrogen bond.

The U6C variant was also predicted to eliminate a single hydrogen bond between the aptamer O4 keto group and the N9 imine of the ligand pyrrolo ring (Fig. 2, *A* and *B*). However, the U6C change introduces a steric block from replacement of a keto with an amine. This substitution may account for the greater relative loss in binding affinity of this variant compared with A29Pur in which a functional group was eliminated. As expected, the U6C change proved detrimental for preQ$_1$ and preQ$_0$, whose K_D values were estimated to be >274 and >199 μM, respectively (Table 3). Like A29Pur, the U6C mutation also has the potential to eliminate two core hydrogen bonds between the Watson-Crick face of U6 and the Hoogsteen edge of A28 (Fig. 2, *A* and *B*).

The 2′-OH group of G11 was observed to be within hydrogen bonding distance of the O6 keto group of preQ$_0$ (Fig. 2*B*) and was perceived to be a potential contributor to metabolite recognition (22). However, this interaction was not present in the preQ$_1$-bound state due to an apparent change in the ribose pucker (Fig. 2, *A* (*inset*) *versus B*). Instead, the G11 ribose hydroxyl is oriented close to the methylamine of preQ$_1$, although it is not in an optimal hydrogen bonding orientation. Mutation of the 2′-OH group of G11 to 2′-deoxy G11 revealed no significant deviation in either preQ$_0$ or preQ$_1$ binding but showed slightly more favorable binding properties (Table 3). The fact that the 2′-deoxy G11 variant had no substantial effects on the binding affinity or kinetics of either metabolite appears to rule out a role for this group in metabolite selectivity.

Mutagenesis of T. tengcongensis Aptamer Base Interactions That Promote PreQ$_1$ Binding but Not PreQ$_0$—A second category of mutants was designed to identify aptamer functional groups that contribute to the higher affinity of preQ$_1$ over preQ$_0$ (2.05 nM *versus* 35.10 nM, respectively; Table 3). The crystal structure of the *T. tengcongensis* aptamer bound to preQ$_1$ provides some insight into this question because the methylamine group is within 4.0 Å of the O6 and N7 groups of conserved base G5 (Figs. 2*A* (*inset*) and 3*B*). However, a sulfate ion bound to the preQ$_1$ methylamine precludes a cogent interpretation (Fig. 3*B*).

Previously, the G5 base was shown to be universally conserved in preQ$_1$ class I aptamers (21). Changes in the J1 stem at position C16 (Fig. 1*A*) as well as flanking base pairs showed poor responses to ligand binding or failed to elicit metabolite-dependent gene regulation (21). Although no functional analysis was reported for G5, *T. tengcongensis* crystal structures bound to metabolites suggested that the substitution of 2,6-diaminopurine (DAP) in the context of the double mutation, G5DAP/C16U, would replace the G5 O6 keto group with an N6 amine. A comparable mutational analysis (21) demonstrated

that this variant adopts a Watson-Crick-like base pair, which provided confidence that the floor of the binding pocket would remain intact. However, the N6 exocyclic amine from DAP is predicted to disrupt hydrogen bonding to the preQ$_1$ methylamine, whereas this interaction cannot occur with preQ$_0$ due to the presence of its linear cyano moiety (Figs. 1*A* and 2, *A* and *B*).

The results revealed K_D values of 2.01 ± 0.33 and 1.63 ± 0.12 μM for preQ$_1$ and preQ$_0$, respectively (Fig. 5*E* and Table 3). The relative losses in affinity suggest a nearly 10^3-fold reduction in preQ$_1$ binding but only a 46-fold loss by preQ$_0$, thus providing evidence for involvement of the G5 O6 keto in binding preQ$_1$ but not preQ$_0$.

DISCUSSION

Riboswitches regulate gene expression by altering accessibility to sequences that signal transcription or translation. Prior structural investigations of the preQ$_1$ riboswitch focused on type II aptamers that function transcriptionally by altering the interconversion of terminator and anti-terminator stem-loops (23–25). Here we examined the structural and functional properties of a type I aptamer from *T. tengcongensis* involved in translational regulation. A32 of the aptamer sequence (Fig. 1*B*) appears to be the start of the RBS based on the Shine-Dalgarno consensus sequence and base-pairing energy with the 16 S rRNA (supplemental Fig. S1). This assignment places the last nucleotide of our construct, G33, as the second base of the RBS (Fig. 1*B*) and has implications for how the mode of preQ$_1$ binding by the *T. tengcongensis* riboswitch can regulate translation.

Crystallographic Conformational Changes Reveal Differences in RBS Accessibility—Comparisons of the preQ$_1$-bound and ligand-free structures of the *T. tengcongensis* riboswitch provide the basis to identify ligand-dependent conformational changes that may lead to RNA-mediated gene regulation. A superposition of these structures revealed changes in and around the binding pocket that suggested the absence of metabolite causes a shift of base A14 such that it interacts with preQ$_1$ binding determinants U6 and A29 (Figs. 2 (*A versus D*) and 3). The position of A14 in the free state coincides with unstacking of bases A32 and G33 of the RBS from the core fold, which increases their solvent accessibility relative to the preQ$_1$-bound state. Although this difference is modest in the context of the crystal lattice, the tangible increase in accessibility (Fig. 3*A*) is illustrative of how the 16 S rRNA of the ribosome could gain greater access to the RBS in the free-state structure, thereby resulting in a "gene-on" state.

Modes of PreQ$_1$ and PreQ$_0$ Binding—The mode of metabolite binding by members of the class I preQ$_1$ riboswitch family appears to be conserved insofar as the *B. subtilis* (type II) and *T. tengcongensis* (type I) aptamer structures utilize a common set of core bases for recognition. Our functional analysis supports the importance of U6 and A29 in recognition of both the preQ$_0$ and preQ$_1$ metabolites (Table 3), thus corroborating crystallographic observations. Efforts to understand the molecular basis for the affinity preference of preQ$_1$ over preQ$_0$ led us to examine the G5DAP/C16U double mutant. Our crystal structure shows close proximity between the preQ$_1$ methylamine and the O6 keto of G5 (Fig. 2*A*, *inset*). However, a sulfate ion from the mother liquor is bound to the methylamine group of preQ$_1$ (Fig. 3*B*), thereby obfuscating its potential for recognition by the aptamer. We hypothesized that substitution of the G5 O6 keto with a DAP N6 amine would sterically occlude binding of the preQ$_1$ methylamine and prevent formation of a hydrogen bond. Differences in the K_D values between preQ$_1$ and preQ$_0$ correspond to a free energy change of 1.68 kcal/mol. This modest difference suggests no more than 1–2 neutral hydrogen bonds (54). Our results for this mutant suggested a slight favorability in preQ$_0$ binding over preQ$_1$, which seems considerable given the 17-fold greater affinity that wild type exhibits for preQ$_1$ over preQ$_0$ (Table 3). Such a trend supports the expectation that the G5DAP mutation is more detrimental for preQ$_1$ than preQ$_0$ due to the steric block created by the DAP N6 amine. Although the deletion of the G5 keto might appear to be a more conservative probe for hydrogen bonding, we examined a G52AP (2-amino-purine) mutant devoid of an O6 keto moiety and measured the K_D for preQ$_1$ at >914 μM (data not shown). Changes in mutant affinity for metabolites relative to wild type suggest that substitutions in the aptamer core have additional long range effects that go beyond energy differences expected for loss of 1–2 core hydrogen bonds.

A comparative structural analysis provided further insight into the basis of preQ$_1$ *versus* preQ$_0$ specificity. Commonalties are apparent in the mode of preQ$_1$ recognition by conserved bases shared by the *T. tengcongensis* aptamer and the known *B. subtilis* aptamer structures. This makes it possible to understand the basis for preQ$_1$ specificity for all class 1 preQ$_1$ riboswitch family members. In each independent *B. subtilis* structure, the methylamine of preQ$_1$ is sufficiently close to the O6 keto and N7 imino of G5 that the metabolite is within hydrogen bonding distance of these groups (23, 24). These interactions are not present when preQ$_0$ is bound to the *T. tengcongensis* aptamer (22) and would account for the observed energy difference that favors preQ$_1$ affinity over preQ$_0$. Although structures of the *B. subtilis* aptamer also show that the preQ$_1$ methylamine is within hydrogen bonding distance of the phosphate backbone, this interaction is not observed in the *T. tengcongensis* aptamer bound to preQ$_1$ (this work) or preQ$_0$ (22). If this interaction were a means of discriminating the cyano group from the methylamine, the additional energetic difference favoring preQ$_1$ binding would be appreciable, adding another ~3 kcal/mol (54). Further experiments will be necessary to establish the degree of conservation that this non-base interaction exhibits among family members and its role in preQ$_1$ affinity relative to preQ$_0$.

Despite the lower affinity of the *T. tengcongensis* aptamer for preQ$_0$ compared with preQ$_1$, the on-rates differ by only 12-fold, whereas the off-rates are comparable with preQ$_0$ dissociating 1.5-fold faster. Kinetic analysis of the QueF nitrile reductase (Fig. 1*A*) from *B. subtilis* showed a K_m of 237 μM with a k_{cat} of 0.69 min^{-1}, which are values comparable with the kinetic constants of other Q synthesis pathway enzymes (16). Assuming that these enzymes operate at steady-state levels and that K_m is a reasonable upper limit for substrate dissociation from the enzyme-substrate complex (55), then it is reasonable that preQ$_0$ concentrations are abundant in the cell at levels far exceeding its measured affinity in the context of the *T. tengcongensis* aptamer (K_D = 35.1 nM). As such, it appears plausible

that the *T. tengcongensis* aptamer could respond to preQ$_0$ in gene regulation. This possibility is in agreement with the prior work of Breaker and colleagues (21), who recognized that the 10-fold affinity difference measured for preQ$_1$ *versus* preQ$_0$ in the context of the *B. subtilis* aptamer could not exclude preQ$_0$ as a physiologically relevant target.

Proposed Model of Translational Attenuation—The *T. tengcongensis* preQ$_1$ riboswitch represents an example of direct translational attenuation by the criteria that the aptamer is located fewer than 15 nucleotides upstream of the start codon (supplemental Fig. S1) and the sequestration of RBS sequences occurs within the aptamer domain (1). The preponderance of investigations on genetic regulation by riboswitches has focused on transcriptional control, thus making the *T. tengcongensis* aptamer a notable exception. Although the cellular concentrations of preQ$_1$ are not available in the literature, we can invoke the known K_m of 390 nM for the *E. coli* tRNA transglycosylase (56), which incorporates preQ$_1$ into tRNA and provides a reasonable upper limit for the metabolite's cellular concentration. Because the *T. tengcongensis* aptamer exhibits a K_D for preQ$_1$ of 2.05 nM (Table 3), it would appear that the aptamer senses preQ$_1$ at concentrations ~200-fold lower than its steady-state consumption level. This seems plausible because the regulated gene product, COG1564, is a putative membrane protein invoked in preQ$_1$ transport (21, 57). Because GTP levels in *E. coli* are as high as 1.3–4.9 mM (58), the cell may need to be significantly depleted of GTP before it abandons *de novo* Q synthesis to undertake preQ$_1$ scavenging. With an off-rate of $1.53 \times 10^{-4}\ s^{-1}$, the half-life for dissociation of preQ$_1$ from the *T. tengcongensis* aptamer is 1.4 h. By contrast, the half-life for decay of the average *E. coli* message is 5 min (59), with individual half-lives ranging from seconds to as long as 1 h (59). This time frame suggests that once preQ$_1$ binds to the *T. tengcongensis* aptamer, the associated mRNA will undergo significant translational attenuation. However, translational attenuation of riboswitches such as the *T. tengcongensis* aptamer must also consider kinetic control. In *E. coli*, transcription and translation are closely coupled via the NusE-NusG protein interaction (32), which would require regulation by the *T. tengcongensis* aptamer to occur at preQ$_1$ levels far above its K_D. Such models require additional testing and validation but are worth considering in light of the different K_D values associated with members of the preQ$_1$ riboswitch family.

Differences in Ligand-induced Conformational Changes among PreQ$_1$ Aptamers from Different Genera—The preQ$_1$ riboswitch represents the first opportunity to compare metabolite-induced conformational changes by aptamers from three different organisms. Prior analysis of the *B. subtilis* and *F. nucleatum* preQ$_1$ riboswitches suggested that aptamer folding was dependent strictly on the presence of ligand (23, 25, 26). Our SAXS analysis of the *F. nucleatum* aptamer supports such a ligand-induced conformational change (Fig. 4), and the associated Kratky analysis suggests only partial folding in the absence of preQ$_1$ (supplemental Fig. S2*D*). This finding is consistent with other free-state analyses of these aptamers in solution that showed formation of a hairpin structure attached to a disordered 3′-tail (23, 26). By contrast, the *T. tengcongensis* aptamer is highly compact in the free state (R_g^P = 17.0 Å, r_{max} = 57 Å) and indicates little change in compactness in the presence of preQ$_1$ (R_g^P = 16.5, r_{max} = 51 Å). These results demonstrate that small riboswitch aptamers can exhibit highly compact free states in contrast to prior assumptions (60) and that variable degrees of ligand-dependent folding among riboswitches of the same class may be commonplace, suggesting that the mechanism of action for a given aptamer must be evaluated on a case-by-case basis (61).

Expectations for Molecular Level Conformational Features in the Free State—Crystal structures of the *T. tengcongensis* aptamer exhibited compact conformations in the bound and free states with dimensions that concur with those measured in solution (Table 2). However, efforts to fit observed and calculated scattering profiles (Fig. 4*A*) revealed that the preQ$_1$-bound state is a significantly better descriptor of the solution conformation (with a χ^2 of 1.7, indicating a reasonable fit (11)) as compared with the free-state structure with a χ^2 of 5.8, which is considered poor (Fig. 4*A*). The discrepancy between the preQ$_1$-free-state crystal structure and the solution data most likely originates from the constraints of the crystal lattice rather than incompleteness of the free-state model, which is missing nucleotide A13 (Fig. 2*C*). Our test calculations indicated that such a deletion has only a nominal effect on χ^2. In contrast, the free-state crystal structure fits better to the preQ$_1$-bound SAXS data than the free-state scattering data. This result is best explained by the similar crystal-packing environments of both crystal forms, which produced r_{max} values of ~51 Å (Table 2). In solution, only the preQ$_1$-bound sample has an r_{max} of 51 ± 5 Å, whereas the free state showed an r_{max} of 57 ± 6 A. This suggests that crystal packing favors a more bound-state-like r_{max}, which may be the main source of the discrepancy in the free-state scattering profiles. An analogous result was observed previously for the SAM I riboswitch in which the SAM-bound state showed a χ^2 value of 1.6 between the crystal structure and solution data, whereas the free-state aptamer had a χ^2 value of 5.1. Like position A14 of the *T. tengcongensis* aptamer, position A46 of the SAM I aptamer moves 7.5 Å in the free state to occlude SAM access (supplemental Fig. S3, *A versus B*) (11).

Although the *T. tengcongensis* and SAM I free-state crystal structures are not adequate descriptors of solution scattering data, it is worth noting some general structural expectations for their free-state conformations. The observation that their ligand-binding pockets are blocked (Fig. 2*D versus* supplemental Fig. S3*B*) also has been observed for free-state crystal structures of the lysine riboswitch (9, 10) and the U65C mutant of the pbuE adenine riboswitch (62). Because such conformations are ill suited to ligand binding, it is most plausible that they are in equilibrium with open states in solution (11). The plausibility of this model came from the conformational ensemble analysis of the SAM-I riboswitch in which both open and closed conformations were required to deconvolute the free-state solution scattering profile, producing a χ^2 value of 0.83 (11). Members of the ensemble exhibited substantial changes in the orientation of helical segments, demonstrating folding differences beyond localized open and closed states. We envision a similar ensemble for the preQ$_1$ riboswitch.

Implications for Long Range Signaling between the Ligand Pocket and the RBS—Our mutagenesis results on various bases in and around the metabolite-binding pocket suggested that single functional group changes often exhibit deleterious binding effects incommensurate with those expected from the loss of 1–2 hydrogen bonds. Investigations of protein and RNA enzymes have shown that changes distant from the active site can influence catalytic function because they are part of an interaction network that limits dynamics and provide proper orientation of catalytic functional groups (63, 64).

It is conceivable that riboswitch aptamers are subject to control by similar interaction networks and that these help sample conformations conducive to ligand binding while maintaining a fold that couples ligand binding to distant regions of the riboswitch. This organization could serve as a basis to control accessibility to gene regulatory sequences, such as the RBS. We favor this interpretation for the *T. tengcongensis* preQ$_1$ riboswitch because a series of interconnected movements were implied by the free-state structure as a result of inserting base A14 into the ligand-binding pocket (Fig. 3*A*, *arrows*). Of special note is the greater accessibility to the RBS in the free-state structure and its apparent uncoupling from the aptamer core through the loss of base stacking. It remains to be seen whether this mode of interaction will be a general phenomenon for riboswitches that utilize direct translation attenuation to regulate gene expression.

Acknowledgments—We thank Nils Walter and Robert Batey for critical remarks on the manuscript. We thank Jason Salter and other members of the Wedekind laboratory for helpful discussions. We thank Clara L. Kielkopf for assistance with SPR, which was obtained through National Institutes of Health Grant RR027241 (to Clara L. Kielkopf). We thank Richard Gillilan and the staff of MacCHESS for assistance with SAXS and crystallography. We thank the staff of SSRL for help with remote data collection. MacCHESS is supported by National Science Foundation Award DMR-0225180 and NCRR, National Institutes of Health, Award RR-01646SSRL. SSRL is operated by Stanford on behalf of the United States Department of Energy. The SSRL Structural Molecular Biology Program is supported by the Department of Energy and by NCRR and NIGMS, National Institutes of Health.

REFERENCES

1. Barrick, J. E., and Breaker, R. R. (2007) *Genome Biol.* **8,** R239
2. Winkler, W. C., and Breaker, R. R. (2005) *Annu. Rev. Microbiol.* **59,** 487–517
3. Irnov Kertsburg, A., and Winkler, W. C. (2006) *Cold Spring Harb. Symp. Quant. Biol.* **71,** 239–249
4. Blount, K. F., and Breaker, R. R. (2006) *Nat. Biotechnol.* **24,** 1558–1564
5. Lee, E. R., Blount, K. F., and Breaker, R. R. (2009) *RNA Biol.* **6,** 187–194
6. Serganov, A. (2010) *RNA Biol.* **7,** 98–103
7. Edwards, A. L., Reyes, F. E., Héroux, A., and Batey, R. T. (2010) *RNA* **16,** 2144–2155
8. Huang, L., Serganov, A., and Patel, D. J. (2010) *Mol. Cell* **40,** 774–786
9. Garst, A. D., Héroux, A., Rambo, R. P., and Batey, R. T. (2008) *J. Biol. Chem.* **283,** 22347–22351
10. Serganov, A., Huang, L., and Patel, D. J. (2008) *Nature* **455,** 1263–1267
11. Stoddard, C. D., Montange, R. K., Hennelly, S. P., Rambo, R. P., Sanbonmatsu, K. Y., and Batey, R. T. (2010) *Structure* **18,** 787–797
12. Ottink, O. M., Rampersad, S. M., Tessari, M., Zaman, G. J., Heus, H. A., and Wijmenga, S. S. (2007) *RNA* **13,** 2202–2212
13. Stoddard, C. D., Gilbert, S. D., and Batey, R. T. (2008) *RNA* **14,** 675–684
14. Grosjean, H., de Crécy-Lagard, V., and Björk, G. R. (2004) *Trends Biochem. Sci.* **29,** 519–522
15. McCarty, R. M., Somogyi, A., Lin, G., Jacobsen, N. E., and Bandarian, V. (2009) *Biochemistry* **48,** 3847–3852
16. Lee, B. W., Van Lanen, S. G., and Iwata-Reuyl, D. (2007) *Biochemistry* **46,** 12844–12854
17. Iwata-Reuyl, D. (2003) *Bioorg. Chem.* **31,** 24–43
18. Hurt, J. K., Olgen, S., and Garcia, G. A. (2007) *Nucleic Acids Res.* **35,** 4905–4913
19. Marks, T., and Farkas, W. R. (1997) *Biochem. Biophys. Res. Commun.* **230,** 233–237
20. Huang, B. S., Wu, R. T., and Chien, K. Y. (1992) *Cancer Res.* **52,** 4696–4700
21. Roth, A., Winkler, W. C., Regulski, E. E., Lee, B. W., Lim, J., Jona, I., Barrick, J. E., Ritwik, A., Kim, J. N., Welz, R., Iwata-Reuyl, D., and Breaker, R. R. (2007) *Nat. Struct. Mol. Biol.* **14,** 308–317
22. Spitale, R. C., Torelli, A. T., Krucinska, J., Bandarian, V., and Wedekind, J. E. (2009) *J. Biol. Chem.* **284,** 11012–11016
23. Kang, M., Peterson, R., and Feigon, J. (2009) *Mol. Cell* **33,** 784–790
24. Klein, D. J., Edwards, T. E., and Ferré-D'Amaré, A. R. (2009) *Nat. Struct. Mol. Biol.* **16,** 343–344
25. Rieder, U., Kreutz, C., and Micura, R. (2010) *Proc. Natl. Acad. Sci. U.S.A.* **107,** 10804–10809
26. Rieder, U., Lang, K., Kreutz, C., Polacek, N., and Micura, R. (2009) *Chembiochem* **10,** 1141–1144
27. Ali, M., Lipfert, J., Seifert, S., Herschlag, D., and Doniach, S. (2010) *J. Mol. Biol.* **396,** 153–165
28. Serganov, A., Polonskaia, A., Phan, A. T., Breaker, R. R., and Patel, D. J. (2006) *Nature* **441,** 1167–1171
29. Thore, S., Leibundgut, M., and Ban, N. (2006) *Science* **312,** 1208–1211
30. Lipfert, J., Das, R., Chu, V. B., Kudaravalli, M., Boyd, N., Herschlag, D., and Doniach, S. (2007) *J. Mol. Biol.* **365,** 1393–1406
31. Wedekind, J. E., and McKay, D. B. (2000) *Methods Enzymol.* **317,** 149–168
32. McCarty, R. M., and Bandarian, V. (2008) *Chem. Biol.* **15,** 790–798
33. Quaranta, D., McCarty, R., Bandarian, V., and Rensing, C. (2007) *J. Bacteriol.* **189,** 5361–5371
34. Davoll, J. (1960) *J. Chem. Soc.*, 131–138
35. Soltis, S. M., Cohen, A. E., Deacon, A., Eriksson, T., González, A., McPhillips, S., Chui, H., Dunten, P., Hollenbeck, M., Mathews, I., Miller, M., Moorhead, P., Phizackerley, R. P., Smith, C., Song, J., van dem Bedem, H., Ellis, P., Kuhn, P., McPhillips, T., Sauter, N., Sharp, K., Tsyba, I., and Wolf, G. (2008) *Acta Crystallogr. D Biol. Crystallogr.* **64,** 1210–1221
36. Otwinowski, Z., and Minor, W. (1997) *Methods Enzymol.* **276,** 307–326
37. Adams, P. D., Gopal, K., Grosse-Kunstleve, R. W., Hung, L. W., Ioerger, T. R., McCoy, A. J., Moriarty, N. W., Pai, R. K., Read, R. J., Romo, T. D., Sacchettini, J. C., Sauter, N. K., Storoni, L. C., and Terwilliger, T. C. (2004) *J. Synchrotron Radiat.* **11,** 53–55
38. Emsley, P., Lohkamp, B., Scott, W. G., and Cowtan, K. (2010) *Acta Crystallogr. D Biol. Crystallogr.* **66,** 486–501
39. DeLano, W. L. (2002) *The PyMOL Molecular Graphics System*, DeLano Scientific, San Carlos, CA
40. CCP4 (1994) *Acta Crystallogr. D Biol. Crystallogr.* **50,** 760–763
41. Ando, N., Chenevier, P., Novak, M., Tate, M. W., and Gruner, S. M. (2008) *J. Appl. Crystallogr.* **41,** 167–175
42. Kabsch, W. (1976) *Acta Crystallogr. Sect. A* **32,** 922–923
43. Konarev, P. V., Volkov, V. V., Sokolova, A. V., Koch, M. H., and Svergun, D. I. (2003) *J. Appl. Crystallogr.* **36,** 1277–1282
44. Feigin, L., and Svergun, D. (1987) *Structure Analysis by Small-Angle X-Ray and Neutron Scattering*, Plenum Press, New York
45. Svergun, D. I. (1992) *J. Appl. Crystallogr.* **25,** 495–503
46. Svergun, D., Barberato, C., and Koch, M. H. (1995) *J. Appl. Crystallogr.* **28,** 768–773
47. Kleywegt, G., Zou, J., Kjeldgaard, M., and Jones, T. (2001) in *International Tables for Crystallography* (Rossmann, M., and Arnold, E., eds) pp. 353–356 and 366–367, Kluwer Academic Publishers, Dordrecht, The Netherlands
48. Myszka, D. G. (1999) *J. Mol. Recognit.* **12,** 279–284
49. Mertens, H. D., and Svergun, D. I. (2010) *J. Struct. Biol.* **172,** 128–141

50. Doniach, S. (2001) *Chem. Rev.* **101,** 1763–1778
51. Lang, K., Rieder, R., and Micura, R. (2007) *Nucleic Acids Res.* **35,** 5370–5378
52. Rieder, R., Lang, K., Graber, D., and Micura, R. (2007) *Chembiochem* **8,** 896–902
53. Smith, K. D., Lipchock, S. V., Ames, T. D., Wang, J., Breaker, R. R., and Strobel, S. A. (2009) *Nat. Struct. Mol. Biol.* **16,** 1218–1223
54. Fersht, A. R., Shi, J. P., Knill-Jones, J., Lowe, D. M., Wilkinson, A. J., Blow, D. M., Brick, P., Carter, P., Waye, M. M., and Winter, G. (1985) *Nature* **314,** 235–238
55. Northrop, D. B. (1998) *J. Chem. Educ.* **75,** 1153–1157
56. Hoops, G. C., Townsend, L. B., and Garcia, G. A. (1995) *Biochemistry* **34,** 15381–15387
57. Meyer, M. M., Roth, A., Chervin, S. M., Garcia, G. A., and Breaker, R. R. (2008) *RNA* **14,** 685–695
58. Bennett, B. D., Kimball, E. H., Gao, M., Osterhout, R., Van Dien, S. J., and Rabinowitz, J. D. (2009) *Nat. Chem. Biol.* **5,** 593–599
59. Celesnik, H., Deana, A., and Belasco, J. G. (2007) *Mol. Cell* **27,** 79–90
60. Zhang, J., Lau, M. W., and Ferré-D'Amaré, A. R. (2010) *Biochemistry* **49,** 9123–9131
61. Baird, N. J., Kulshina, N., and Ferré-D'Amaré, A. R. (2010) *RNA Biol.* **7,** 328–332
62. Delfosse, V., Bouchard, P., Bonneau, E., Dagenais, P., Lemay, J. F., Lafontaine, D. A., and Legault, P. (2010) *Nucleic Acids Res.* **38,** 2057–2068
63. Rueda, D., Bokinsky, G., Rhodes, M. M., Rust, M. J., Zhuang, X., and Walter, N. G. (2004) *Proc. Natl. Acad. Sci. U.S.A.* **101,** 10066–10071
64. Forconi, M., Sengupta, R. N., Piccirilli, J. A., and Herschlag, D. (2010) *Biochemistry* **49,** 2753–2762
65. García De La Torre, J., Huertas, M. L., and Carrasco, B. (2000) *Biophys. J.* **78,** 719–730
66. Praaenikar, J., Afonine, P. V., Guncar, G., Adams, P. D., and Turk, D. (2009) *Acta Crystallogr. D Biol. Crystallogr.* **65,** 921–931